

Journal of Materials Chemistry A

Materials for energy and sustainability

Accepted Manuscript

This article can be cited before page numbers have been issued, to do this please use: M. Du, B. Nan, Y. Li, L. Zhengwu, K. Hou, Y. Qin, G. Zheng, Z. Liang, L. Zhang, D. Wang, L. Guo, L. Jiang, T. Chen, P. Fan, N. Sun and L. Li, *J. Mater. Chem. A*, 2025, DOI: 10.1039/D5TA05111H.



This is an Accepted Manuscript, which has been through the Royal Society of Chemistry peer review process and has been accepted for publication.

Accepted Manuscripts are published online shortly after acceptance, before technical editing, formatting and proof reading. Using this free service, authors can make their results available to the community, in citable form, before we publish the edited article. We will replace this Accepted Manuscript with the edited and formatted Advance Article as soon as it is available.

You can find more information about Accepted Manuscripts in the [Information for Authors](#).

Please note that technical editing may introduce minor changes to the text and/or graphics, which may alter content. The journal's standard [Terms & Conditions](#) and the [Ethical guidelines](#) still apply. In no event shall the Royal Society of Chemistry be held responsible for any errors or omissions in this Accepted Manuscript or any consequences arising from the use of any information it contains.

In-situ generation of the spinel structural FeCr_2O_4 catalyst for CO_2 -assisted ethane oxidative dehydrogenation

View Article Online
DOI: 10.1039/D5TA05111H

Meng Du^{a,b,c}, Bing Nan^{a,b*}, Yunan Li^{a,c}, Zhengwu Liu^{a,c}, Kunming Hou^b, Yulin Qin^b, Guanhaojie Zheng^b, Zhenye Liang^{a,c}, Lina Zhang^b, Daolei Wang^d, Lingling Guo^b, Luozhen Jiang^b, Chen Tian^b, Peng Fan^b, Nannan Sun^{b*}, Lina Li^{a,b*}

^a Shanghai Institute of Applied Physics, Chinese Academy of Sciences, Shanghai 201204, China

^b Shanghai Advanced Research Institute, Chinese Academy of Sciences, Shanghai 201210, China

^c University of Chinese Academy of Sciences, Beijing 100049, China

^d Division of China, TILON Group Technology Limited, Shanghai, China.

*Corresponding author. E-mail: nanb@sari.ac.cn (B. Nan); sunnn@sari.ac.cn (N. Sun); lilina@sinap.ac.cn (L. Li).



Abstract

View Article Online
DOI: 10.1039/D5TA05111H

Ethylene (C_2H_4) is a crucial raw material for the chemical industry. Recently, the oxidative dehydrogenation of ethane (C_2H_6) using CO_2 as a milder oxidant (CO_2 -ODHE) has been proposed as a potential method for C_2H_4 production through the efficient utilization of shale gas and the mitigation of CO_2 emissions. In this work, a series of Fe, Cr-Fe, and Cr oxides were prepared by a two-step urea precipitation method with Fe_3O_4 , $FeCr_2O_4$, and Cr_2O_3 components, in which the Cr-Fe catalyst exhibits better activity with the conversion of ethane (35%) and CO_2 (27%) and stable C_2H_4 yield (18%) at 650 °C. Through TEM, SEM, Raman, XAFS and in-situ XRD results, it was found that the in-situ formation of the $FeCr_2O_4$ during the CO_2 -ODHE reaction can enhance the thermostability of the Cr-Fe catalyst. Furthermore, the generation of $FeCr_2O_4$ effectively adsorbs and activates CO_2 molecules to reduce the generation of deposited carbon on the surface of the Cr-Fe catalyst.

Key words: CO_2 -ODHE, Cr-Fe oxides Catalysts, Anti-coking, $FeCr_2O_4$, C_2H_4



1. Introduction

View Article Online
DOI: 10.1039/D5TA05111H

Ethylene (C_2H_4) is recognized as the cornerstone of the petrochemical industry, serving as a crucial intermediate for over 70% of fundamental organic chemical raw materials, including ethylene oxide, polypropylene, and polystyrene, which are widely applied in textiles, plastics, and other fields^{1, 2}. With the recent continuous increase in verified shale gas reserves, the catalytic dehydrogenation of light alkanes, which constitute more than 20% of shale gas, has emerged as a promising and economically efficient pathway for ethylene production^{3, 4}. The oxidative dehydrogenation of ethane using CO_2 (CO_2 -ODHE) refers to the process with CO_2 as a mild oxidant to produce ethylene with lower energy consumption and a higher reaction equilibrium constant⁵ and eliminate carbon deposition⁶ by providing reactive oxygen species ($*O$). CO_2 can react with coke deposited on the catalyst surface via the Boudouard reaction ($CO_2 + C = 2CO$), thus improving catalyst performance. Furthermore, taking into account both thermodynamic and kinetic factors, the CO_2 -ODHE process needs to be conducted at high temperatures (> 873 K), which results in several problems such as poor high-temperature stability, susceptibility to sintering⁷, and carbon deposition, hindering their industrial applications⁸. However, the sintering of the active species at high reaction temperatures can lead to irreversible deactivation of the catalysts.⁹ In addition, the side reactions, such as the reforming reaction and the reverse water gas shift (RWGS) reaction, can significantly influence the overall catalytic performance. The reforming reaction with the conversion of alkanes into syngas (CO and H_2) competes with the desired dehydrogenation pathway, leading to reduced ethylene selectivity and yield¹⁰. On the other hand, the RWGS reaction ($CO_2 + H_2 \leftrightarrow CO + H_2O$) can promote the reaction equilibrium by consuming H_2 ⁵. Therefore, developing efficient catalysts with excellent catalytic performance, sintering resistance, and anti-coking properties for the CO_2 -ODHE reaction has received wide research for both academic and practical significance.

Recently, a series of typical non-noble metal CO_2 -ODH catalysts have been widely developed, such as Cr-, Ga-, and Fe-based oxides^{5, 11-15}. Chromium-based catalysts are the most widely studied active components in this field in the CO_2 -ODHE reaction because of their high activity and selectivity, which can



make a recycle between metallic and oxidized Cr species to adsorb and activate CO₂ for the dehydrogenation of C₂H₆¹⁶. Both the inevitable toxicity of Cr⁶⁺ and the easy aggregation of Cr₂O₃ further restrict the application of Cr-based catalysts in the CO₂-ODHE reaction¹⁷. In addition, Fe, as a typical promoter, is frequently used to modify active metals (Cr, Co, or Ni) by altering electronic and coordination structures. Yan et al.¹⁸ found that the Ni-FeO_x interface sites can selectively break C-H rather than C-C bonds in C₂H₆ to promote the formation of C₂H₄. Furthermore, the Fe³⁺/Fe²⁺ redox cycle and unique α-Fe component can also effectively prevent reforming reactions¹⁹. Recently, FeCr₂O₄ with a unique spinel structure has received a wide attention because of its good conductivity, reducibility, and thermodynamic stability, which has been evidenced as an excellent participate for high-temperature reaction^{9, 20}. Besides, according to kinetic experimental and DFT studies, FeCr₂O₄ could activate the sp² C-H bond activation of benzene with lower activation energy compared to the Cr₂O₃ component²¹. Bogdan et al. studied carbon-supported Fe-Cr-Ni and Fe-Cr oxide catalysts, discovering that the formation of the FeCr₂O₄ phase on the surface of Fe-Cr/C catalysts is responsible for the high stability and high ethylene selectivity at 700 °C²²⁻²⁴. And in another work, they found that the formation of FeCr₂O₄ could prevent the reduction of iron and the formation of iron carbides²⁵. Additionally, in their latest research, it was found that a reversible water-gas shift reaction is activated by spinel-type oxide phases, which was characterized in detail by in situ magnetometry and Mössbauer spectroscopy methods²⁶. While these studies highlight the beneficial role of the supported FeCr₂O₄ phase, the potential for its in-situ generation during the demanding CO₂-ODHE reaction itself, and its subsequent impact on catalytic performance and stability, remain less explored. Thus, we investigate the structural evolution of FeCr oxide catalysts under CO₂-ODHE conditions, specifically focusing on whether the beneficial FeCr₂O₄ spinel phase forms in situ during the reaction and how this dynamic process governs catalytic behavior.

Here, we synthesized nano iron oxide, chromium oxide, and FeCr bimetallic oxides using a two-step urea precipitation method and applied them in the CO₂-ODHE reaction. Through a series of structural characterizations such as XRD, SEM, TEM, Raman, XAFS, and temperature-programmed experiments, we



found that the spinel structural FeCr_2O_4 , which is formed in situ under the reaction atmosphere, exhibited good thermal stability to endure the high reaction temperature. Meanwhile, the FeCr_2O_4 could enhance the adsorption and activation of CO_2 to mitigate coke accumulation and improve the activity.

2. Experimental

2.1. Catalyst preparation

Without any additional purification, all of the chemicals utilized in this work were analytical grade and bought from Sinopharm Chemical Reagent Co., Ltd.

The catalysts used in this study were synthesized using a two-step urea hydrolysis co-precipitation method. Ferric nitrate ($\text{Fe}(\text{NO}_3)_3 \cdot 9\text{H}_2\text{O}$) and chromium nitrate ($\text{Cr}(\text{NO}_3)_3 \cdot 9\text{H}_2\text{O}$) were chosen as the metal precursors. The metal ion ratios were controlled at 1:0, 1:3, and 0:1, respectively. The metal nitrates were mixed, stirred, and dissolved in deionized water. The mixture was aged for 1 h and then transferred to a 100 mL polytetrafluoroethylene (PTFE)-lined autoclave. The autoclave was first maintained at 80 °C in an oven for 6 h and then heated to 180 °C for 24 h. Afterward, the autoclave was allowed to cool naturally to room temperature. The resulting precipitates were collected by multiple centrifugations and washed with deionized water until the pH reached 7. The final products were dried in a vacuum oven at 70 °C and then calcined at 400 °C for 4 h with a heating rate of 10 °C·min⁻¹. The fresh samples obtained were designated as Fe, Cr-Fe, and Cr, respectively.

2.2. Characterization

The nitrogen adsorption-desorption isotherm was analyzed on an ASAP2020-HD88 analyzer (Micromeritics Co., Ltd.) at 77 K. Before introducing N_2 , the measured powders were degassed at 250 °C for 4 h under vacuum (<100 μm Hg). The pore-size distribution of each sample was calculated using the BJH method in accordance with the desorption branch of the obtained isotherms. The BET specific surface areas were calculated from data in the relative pressure range between 0.06 and 0.30.



The powder X-ray diffraction (XRD) patterns were obtained using Cu $K_{\alpha 1}$ radiation ($\lambda = 1.540598 \text{ \AA}$) with a scanning range of 10° - 90° on a Panalytical Empyrean X-ray diffractometer (40 kV and 40 mA). Prior to each test, the ground sample was planished on a quartz sample holder.

The transmission electron microscopy (TEM), high-resolution transmission electron microscopy (HRTEM) images and scanning transmission electron microscopy-energy dispersive spectrometer (STEM-EDS) elemental mapping results were measured on a FEI TALOS F200X microscope with an acceleration voltage of 200 kV. The measured samples were first ultrasonically dispersed in pure alcohol for about 5 min, and then a drop of the liquid supernatant was applied to a very thin carbon film. Before being placed inside the sample holder, the sample grid was allowed to dry naturally. The scanning electron microscope (SEM) images were obtained from a field emission scanning electron microscope (Zeiss, sigma500).

The X-ray photoelectron spectroscopy (XPS) for the used samples was performed by PHI 5000 Versa Probe III with a monochromatic Al K_{α} X-ray source with the beam size of $100 \text{ \mu m} \times 1400 \text{ \mu m}$. Charge compensation was achieved by the dual beam charge neutralization and the binding energy was corrected by setting the binding energy of the hydrocarbon C 1s feature to 284.8 eV.

The Raman spectra were collected using a Renishaw Raman InVia reflex microscope with laser excitation at 532 nm. The samples were attached to a glass slide, and Raman shifts were acquired from 100 to 1900 cm^{-1} with a spectral resolution of 1 cm^{-1} . For each experimental run, the scanning parameter for each Raman spectra was set at 100 s in order to improve the signal-to-noise ratio. In order to assess the repeatability of the spectral results, several spot analyses were performed on various regions of the same sample.

The X-ray absorption fine structure (XAFS) spectra at the Fe K-edge ($E^0 = 7112 \text{ eV}$) and Cr K-edge ($E^0 = 5989 \text{ eV}$) were performed at BL14W1 and 16U1 beam line of Shanghai Synchrotron Radiation Facility (SSRF) operated at 3.5 GeV under “top-up” mode with a constant current of 220 mA. The XAFS data were recorded under transmission mode. The energy was calibrated according to the absorption edge of pure Fe and



Cr foil. The data were analyzed using the Demeter software package²⁷. For the X-ray absorption near edge structure (XANES) part, the experimental absorption coefficients as function of energies $\mu(E)$ were processed by background subtraction and normalization procedures, and reported as “normalized absorption”. The chemical valence of Fe was determined with the linear combination fit by comparison to the corresponding references of Fe/Fe₃O₄ based on the normalized XANES profiles in the Athena software. For the extended X-ray absorption fine structure (EXAFS) part, the Fourier transformed (FT) data in R space were analyzed by multiple Fe compound models for Fe-O, Fe-O-Fe or Fe-O-Cr shells, respectively. The passive electron factors, S_0^2 , were determined by fitting the experimental Fe foil data and fixing the Fe-Fe coordination number (CN) to be 8+6, and then fixed for further analysis of the measured samples. For Cr, the Fourier transform (FT) in R-space is analyzed by applying Cr₂O₃ and Cr₂FeO₄ models to Cr-O and Cr-O-Cr, respectively. Similarly, amp was obtained by fixing the coordination number (CN) of Cr-Cr as 6 according to the data of Cr foil, and then S_0^2 was fixed to further analyze the measured samples. The parameters describing the electronic properties (e.g., correction to the photoelectron energy origin, E_0) and local structure environment including coordination number (CN), bond distance (R) and Debye Waller ($D.W.$) factor around the absorbing atoms were allowed to vary during the fitting process. The fitted ranges for k were selected to be $k = 3.0\text{--}12.0 \text{ \AA}^{-1}$ and $2.8\text{--}11.0 \text{ \AA}^{-1}$ (k^3 weighted) for Fe and Cr samples. The Fourier transformed (FT) data in R space were analyzed by selecting $R = 1.0\text{--}3.4$ and $1.2\text{--}3.0 \text{ \AA}$ (k^3 weighted), respectively.

In-situ X-ray diffraction (XRD) measurements of Cr-Fe catalysts was carried out within a compact flow cell at BL02U2 beam line of Shanghai Synchrotron Radiation Facility (SSRF) ($\lambda = 0.79743 \text{ \AA}$). Two-dimensional XRD data were acquired by using a Pilatus 2M with a distance c.a. 240 mm from the samples. The catalyst sample was compressed into a disc with a diameter of 10 mm and then placed on the heating stage of the in-situ cell. It was reduced in-situ by a mixture of H₂/Ar (20/20 mL·min⁻¹) with the temperature ramping from room temperature to 450 °C (40 °C·min⁻¹) and holding for 30 min. After flushing in Ar for 10 min, the catalyst was sequentially exposed to the reaction gases (CO₂/C₂H₆/Ar = 10/10/20 mL·min⁻¹), and



then temperature was increased to 500, 600, 650, 700 °C (10 °C·min⁻¹), respectively. Each temperature point was maintained for 15 min. The two-dimensional (2D) diffraction images were continuously collected by Pilatus3 S-2M detector. LaB6 standard was used for wavelength calibration. The 2D images were subsequently integrated by the program Dioptas to obtain XRD profiles, The 2θ Angle was converted to the corresponding value of the Cu K_{α1} radiation (λ = 1.54056 Å).

The temperature-programmed reduction by hydrogen (H₂-TPR) measurements for the catalyst samples were conducted on Micromeritics Autochem II 2920 instrument equipped with a thermal conductivity detector (TCD). After being pretreated under O₂ (5%O₂/He) flow in a quartz U-tube reactor at 300 °C for 30 min, the samples (50 mg) were cooled down to room temperature in Ar. Then 5% H₂/Ar (50 mL·min⁻¹) was introduced to pass through the catalyst bed until a stable TCD signal was observed. Subsequently, a temperature ramping program from room temperature to 800 °C at the rate of 10 °C·min⁻¹ was performed.

CO₂-temperature programmed desorption (CO₂-TPD) was carried out on an AutoChem II 2920 (Micromeritics, USA) instrument and a mass spectrometer (LC-D200M, TILON) was used to gather gas signals. 100 mg of fresh catalyst was placed in a U-shaped quartz sample tube. Prior to TPD studies, the catalyst sample was processed with 5% H₂/Ar (50 mL·min⁻¹) at 450 °C for 90 min and then cooled down to room temperature using the same steam. He started purging for 30 min, then the catalyst was exposed to 5% CO₂/He (50 mL·min⁻¹) for 1h until surface saturation was achieved. The weakly physisorbed CO₂ was purged by flushing in He (50 mL·min⁻¹) for 30 min. Finally, desorption of CO₂ was carried out with increasing temperature to 700 °C at a ramp of 10 °C·min⁻¹ under He. The signals of He (m/z = 4) and CO₂ (m/z = 44) were detected by using the mass spectrometer during the investigation.

CO₂-temperature programed surface reaction (CO₂-TPSR) experiments were performed to prove oxidation of deposited carbon by CO₂ for used catalysts (85 mg) on the similar instrument with CO₂-TPD. After being pretreated under He (30 mL·min⁻¹) in a quartz U-tube reactor at 150 °C for 30 min, the samples were cooled down to room temperature in He. Then 5% CO₂/He (30 mL·min⁻¹) was introduced to pass through



the catalyst bed until a stable TCD signal was observed. Subsequently, a temperature ramping program from room temperature to 900 °C at rate of 10 °C·min⁻¹ was performed under 5% CO₂/He flow. The signals of He (m/z = 4) and CO₂ (m/z = 44) were detected by using the mass spectrometer during the investigation. He-TPSR experiments were conducted to prove the intrinsic active oxygen species for coke elimination of the used catalysts (50 mg), following the same procedure as the CO₂-TPSR experiments, with the only difference being that the CO₂ flow was replaced by a He flow.

The TPO experiment was performed using a thermoanalyzer (Setaram Labsys Evo 1150) coupled with a mass spectrometer for evolved gas analysis to quantify the amount of coke deposited on the used catalysts after CO₂-ODHE at 700 °C. The ~10 mg catalyst was placed in a 70 µL alumina crucible and heated in 40-800 °C (5 °C·min⁻¹) under 20% O₂/N₂ flow (40 mL·min⁻¹). The amount of CO₂ in the outlet gas was quantified by an online mass spectrometer.

2.3. Catalytic tests

The catalytic performance of the samples in CO₂-ODHE was evaluated in a 6 mm fixed-bed micro-reactor. 100 mg of catalyst was used in each test. The catalyst was fixed in the middle of the bed with quartz cotton, and the reaction temperature of the catalyst was monitored by a thermocouple located in the center of the bed. Before the catalytic performance test, the catalysts were pretreated at 450 °C in a 50% H₂/Ar flow for 1 hour, then the reaction was initiated by feeding a mixture gas with C₂H₆/CO₂/Ar = 10:10:20 mL·min⁻¹ under atmospheric pressure, N₂ was used as the internal standard. The reaction temperature ranged from 500 to 700 °C, with a step increment of 50 °C. Each temperature point was maintained for 40 min to ensure the reliability and repeatability of the gas chromatography data, allowing us to obtain activity data for the catalysts at different temperatures. The samples after reaction were designated as Fe-used, Cr-Fe-used, and Cr-used, respectively.

The reaction products were analyzed by a gas chromatograph (Agilent Technologies 7890B), using a flame ionized detector (FID) equipped with an Alumina capillary column to detect CH₄, C₂H₆, and C₂H₄(N₂



carrier gas), and a thermal conductivity detector (TCD) packed Porapak Q columns, N columns and molecular sieve 5A columns to detect H₂, N₂, CO, CH₄, and CO₂ (He carrier gas). C₂H₆ conversion (X(C₂H₆)), CO₂ conversion (X(CO₂)), C₂H₄ yield (Y(C₂H₄)), C₂H₄ selectivity (S(C₂H₄)), CO selectivity (S(CO)) and CH₄ selectivity (S(CH₄)) in gaseous products and Carbon balance are calculated as follows:

$$X(C_2H_6) = [F(C_2H_6, \text{in}) - F(C_2H_6, \text{out})] / F(C_2H_6, \text{in}) * 100\%,$$

$$X(CO_2) = [F(CO_2, \text{in}) - F(CO_2, \text{out})] / F(CO_2, \text{in}) * 100\%,$$

$$Y(C_2H_4) = F(C_2H_4, \text{out}) / F(C_2H_6, \text{in}) * 100\%,$$

$$S(C_2H_4) = Y(C_2H_4) / X(C_2H_6) * 100\%,$$

$$S_{\text{gas}}(C_2H_4) = 2 * F(C_2H_4, \text{out}) / [2 * F(C_2H_4, \text{out}) + F(CO, \text{out}) + F(CH_4, \text{out})] * 100\%,$$

$$S_{\text{gas}}(CH_4) = F(CH_4, \text{out}) / [2 * F(C_2H_4, \text{out}) + F(CO, \text{out}) + F(CH_4, \text{out})] * 100\%,$$

$$S_{\text{gas}}(CO) = F(CO, \text{out}) / [2 * F(C_2H_4, \text{out}) + F(CO, \text{out}) + F(CH_4, \text{out})] * 100\%,$$

$$\text{Carbon balance} = [2 * F(C_2H_6, \text{out}) + 2 * F(C_2H_4, \text{out}) + F(CH_4, \text{out}) + F(CO_2, \text{out}) + F(CO, \text{out})] / [2 * F(C_2H_6, \text{in}) + F(CO_2, \text{in})] * 100\%,$$

where $F(i, \text{in})$ and $F(i, \text{out})$ stand for the volume flow of component i (mL·min⁻¹) after N₂ correction at inlet and outlet, respectively.

$$F(i) = F_{(N_2)} * A(i) / A_{(N_2)} * R(i) / R_{(N_2)}$$

$A(i)$: Peak area of component i in the gas chromatogram.

$R(i)$: Relative response factor of component i (determined by calibration with standard gases.).

In the comparison of ethylene formation rates, the effects of space velocity and inert gas dilution have been excluded through the following calculation formula:

$$\text{Rates of Ethylene formation } (\mu\text{mol g}^{-1} \text{ cat s}^{-1}) = Y(C_2H_4) * \text{space velocity (GHSV)} * (V_{C_2H_6} / V_{\text{total}}) / V_m$$



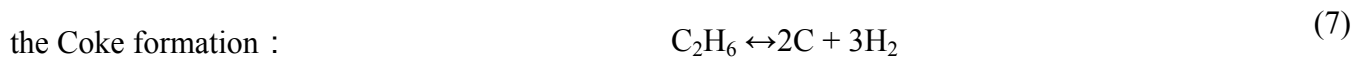
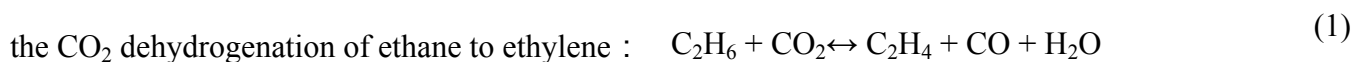
3. Results and discussion

3.1. CO₂-ODHE Catalytic Reaction Performance

View Article Online
DOI: 10.1039/D5TA05111H

In this work, a series of monometallic and bimetallic iron-chromium oxide catalysts, were evaluated by a CO₂-assisted ethane dehydrogenation reaction. Typically, the catalytic performance of samples with different Cr/Fe ratios was tested to optimize the catalyst (Fig. S1). The Cr-Fe (3:1) sample with the highest ethylene yield was selected for comparison with monometallic samples to investigate the structure-activity relationship.

During the CO₂-ODHE, C₂H₄, CH₄, CO, H₂, H₂O, and C products are formed according to following reactions^{18, 28, 29}:



The main and side reactions collectively determine the overall material balance and reaction activity. The results of catalytic experiments and the mass ratio of products at 650 °C are shown in Fig.1 and Table S1. As the temperature increased, Cr-Fe bimetallic sample exhibited much better activity compared with the monometallic Fe and Cr samples. At 650 °C, the conversion of ethane and CO₂ approached 35% and 27%, respectively. The product mass content, with CO constituting 61% and ethylene accounting for 23%, while coke formation represents only 5%, indicates that the Cr-Fe sample is a promising catalyst for the ethane oxidative dehydrogenation reaction. Although monometallic Cr catalyst exhibited 20% for ethane conversion at 650 °C, consistent with unsupported Cr-based catalysts even at a lower space velocity of 3600 mL g⁻¹ cat h⁻¹,^{17, 12}, both the CO₂ conversion and ethylene yield were significantly lower compared to the Cr-Fe catalyst.



Additionally, the significant amount of coke deposited on the monometallic Cr catalyst (accounting for 66% of the mass content) clearly indicates the rapid occurrence of coke formation under high-temperature conditions. Meanwhile, monometallic Fe catalyst exhibited poor catalytic performance in the CO₂-ODHE reaction, only achieving the conversion of both C₂H₆ and CO₂ below 5%, which demonstrated the bad ability to activate the C-H and C-O bonds even at such a high temperature about 650 °C. Supported monometallic Fe-based catalysts in previous studies., such as Fe/CeO₂ and Fe/Mo₂C, exhibit very low ethane conversion of only 0.5%¹⁸ and 8%³⁰ at 600 °C, respectively. Carbon balance for all the experiments reached above 95 % except monometallic Cr catalysts at 650 °C was only 89 % (Fig. 2), and no C₃, C₄, or aromatics were detected. Since the formation of coke is related to the reaction time, we calculated the selectivity of C₂H₄, CO, and CH₄ in the gas-phase products as the temperature increased for different catalyst samples based on the carbon balance data, as shown in Fig.2. At the initial temperature of 500 °C, the ethylene selectivity of the Cr-Fe bimetallic oxide sample was about 56.7%, with low conversion of C₂H₆ and CO₂. As the conversion increased with temperature, the ethylene selectivity in gas-phase products decreased to 40% at 650 °C due to the occurrence of side reactions. Although the ethylene selectivity of the monometallic Cr sample improved at 650 °C, the decline in carbon balance data indicated significant coke formation (Fig. 2b). However, taking the conversion and selectivity into consideration, the highest C₂H₄ yield can be acquired for Cr-Fe samples, reaching nearly 18% at 650 °C (Fig. 1d), almost the same as at 700 °C (Fig. S2). This indicates that the Cr-Fe sample exhibits excellent catalytic activity at 600-650 °C, comparable to the ethane conversion and ethylene yields of various Cr-based and Fe-based catalysts reported in the literature (Table S2). In order to exclude the influence of space velocity and inert gas dilution on the inherent activity, the reaction rates normalized by catalyst weight were calculated. As shown in Table S1, the formation rate of ethylene of the Cr-Fe catalyst was about 13.4 μmol g⁻¹ cat s⁻¹, which was about 6 ~7 times higher than that of other reported Fe- and Cr-based catalysts. Considering the low active metal content in supported catalysts, even when normalized to a single active metal, the ethylene formation rate of the Cr-Fe sample remains comparable to others.



Furthermore, on the basis of stability tests at 650 °C, a slight decrease in the conversion of C₂H₆ and CO₂ was observed. However, the C₂H₄ yield remained at 18% for 300 min.

View Article Online
DOI: 10.1039/D5TA05111H

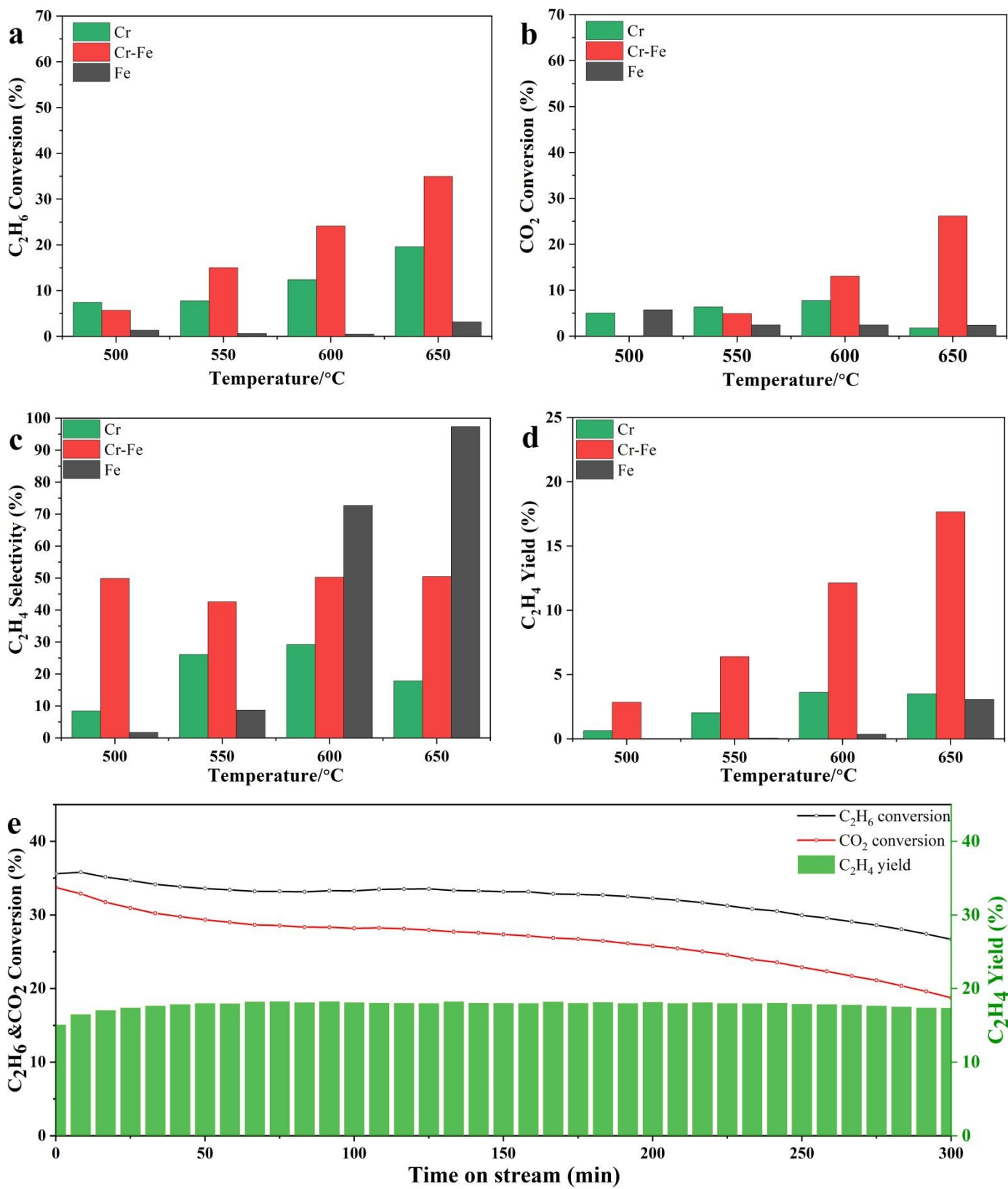


Fig. 1. Catalytic performance of the CO₂-ODHE reaction of Cr, Cr-Fe, and Fe. (a) C₂H₆ conversion, (b) CO₂ conversion, (c) C₂H₄ selectivity, (d) C₂H₄ yield, (e) Stability at 650 °C of Cr-Fe Samples (space velocity: 24,000 mL g⁻¹ cat h⁻¹)

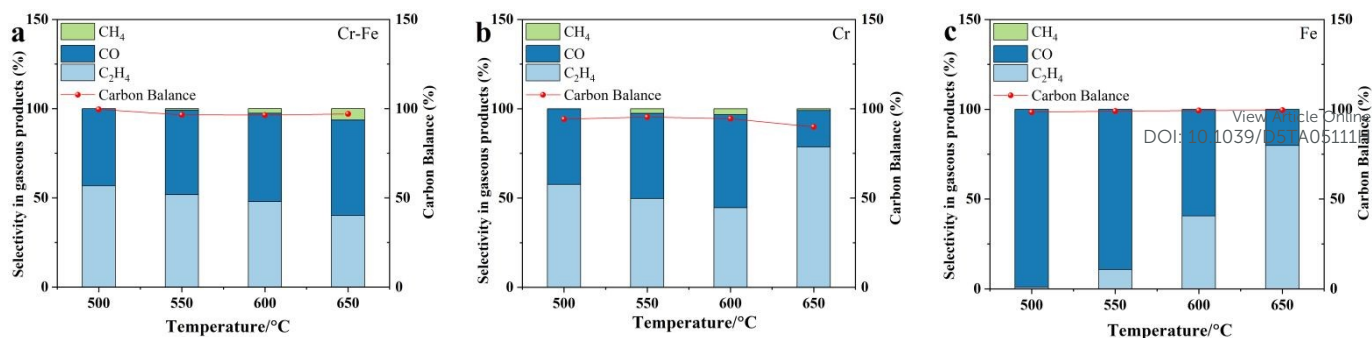


Fig. 2. Selectivity in gaseous products and Carbon balance of (a) Cr-Fe, (b) Cr, and (c) Fe.

3.2. Morphological and Structural Analysis Before and After Reaction

On the basis of the dramatic difference in catalytic performance between Fe, Cr-Fe, and Cr samples, it is significant to figure out the active site and make clear the “structure-activity” relationship in CO₂-ODHE reaction. The powder XRD patterns of the fresh samples were shown in Fig. 3a. The monometallic Fe sample exhibits the hexagonal structure of hematite-type Fe₂O₃ (JCPDS No.99-0060), according to the diffraction peaks at 24.2°, 33.2°, and 35.6°. Meanwhile, the peaks at 24.5°, 33.6°, and 36.2° also demonstrated a typical hexagonal structure of eskolaite-type Cr₂O₃ (JCPDS No.38-1479) for the monometallic Cr sample. The XRD pattern of the Cr-Fe sample was different from the patterns of Fe₂O₃ and Cr₂O₃, which can be attributed to mixed oxide (Fe,Cr)₂O₃ (JCPDS No. 35-1112). Taking into consideration that the atomic ratio for Cr to Fe was 3:1, the main diffraction peaks (104) and (110) of the fresh Cr-Fe sample were closer to the peak positions of the Cr₂O₃ in Fig. 3b. It indicated that Fe³⁺ ions were successfully doped into the Cr₂O₃ lattice to form (Fe,Cr)₂O₃ oxide solid solution in fresh Cr-Fe sample, because of the similar ionic radiuses of the Fe³⁺ (0.645 Å) and Cr³⁺ (0.615 Å) cations³¹. XRD peak broadening is mainly related to the inhomogeneity of the cell size resulting from spatial variations in the amount and distribution of cations and vacancies in Cr³⁺ and Fe³⁺³². Consequently, all three samples exhibited the same hexagonal lattice structure. Furthermore, the average particle sizes of all fresh samples were calculated by the Scherrer formula, about 48 nm, 28 nm, and 24 nm for Fe, Cr-Fe, and Cr sample, respectively. It exhibited monometallic Cr sample possesses the better anti-sintering ability compared to monometallic Fe sample, which can also explain the smaller particle size of fresh Cr-Fe sample due to the formation of a (Fe,Cr)₂O₃ solid solution. Thus, the formation of the (Fe,Cr)₂O₃ solid



solution oxide leads to lattice distortion and an increase in lattice defects, inhibiting grain growth and reducing the grain size of Cr-Fe samples. The smaller grain size indicates more exposed active sites, which is beneficial for catalytic reactions.

Taking the high reaction temperature and complex gas atmosphere of CO₂-ODHE reaction into consideration, dramatic structural evolution may occur during the reaction. From the XRD patterns of all used samples (Fig. 3c), it is evident that the CO₂-ODHE reaction induces significant phase transformations in the Fe-containing catalyst samples. For the Fe-used sample, the peaks at 18.4°, 30.2°, and 35.3° can be attributed to the (111), (220), and (311) planes of cubic phase Fe₃O₄ (JCPDS No.99-0073). It indicated that Fe₂O₃ was reduced to Fe₃O₄ during H₂ pre-activation and the reaction process. Using the Scherrer formula, the grain size of the monometallic Fe sample was ~60 nm after the reaction, suggesting the obvious agglomeration along with the phase transformation during the reaction. For the monometallic Cr sample (initial phase: Cr₂O₃), the XRD pattern demonstrated the stability of Cr₂O₃ phase after the H₂ pre-activation and the reaction process. However, the particle size of Cr₂O₃ increased notably from 24 nm to 36 nm after reaction. For Cr-Fe-used sample, there were new diffraction peaks at 18.3°, 30.1°, 35.5°, 43.1°, 57.1° and 62.6°, indicating the formation of spinel structure FeCr₂O₄ component (JCPDS No.99-0030) with an average particle size of 20.8 nm³³. Compared with used monometallic Fe and Cr samples, the FeCr₂O₄ component exhibited a better anti-sintering ability. In addition, there was also isolated Cr₂O₃ phase in Cr-Fe-used sample due to the high ratio of Cr/Fe about 3:1. Thus, it can preliminarily determinate that the formation of FeCr₂O₄ could improve the catalytic activity of Cr-Fe sample in CO₂-ODHE reaction. Additionally, the material synthesized with the initial Cr/Fe molar ratio of 2:1 was also evaluated to identify the main active phase during the reaction. It was observed that at 650 °C, the ethane conversion (34%), CO₂ conversion (26%), and ethylene yield (17%) over the 2:1 catalyst were largely consistent with those of the 3:1 catalyst (Fig. S1). Furthermore, even in the Cr₂Fe₁-used sample, a small amount of Cr₂O₃ was detected by XRD (Fig. S3), indicating incomplete consistency with the initial stoichiometric ratio. Nevertheless, the similar catalytic performance between both



samples strongly supports that the active species is the spinel-structured FeCr_2O_4 , despite the notably lower content of Cr_2O_3 in the Cr_2Fe_1 -used sample compared to the Cr_3Fe_1 -used sample.

View Article Online
DOI: 10.1039/D5TA05111H

Table 1. Surface Atomic Ratio, BET Surface Area, BJH Pore Size Distribution (r_p), Crystallite Size of fresh FeCrO_x Catalysts and Phase composition, Crystallite Size of used FeCrO_x Catalysts

Sample	Surface atomic ratio (Fe/Cr) ^a	S_{BET} (m^2/g) ^b	r_p (nm) ^b	D_{fresh} (nm) ^c	Phase composition after reaction	D_{used} (nm) ^d
Fe	100/0	13	44.75	48	Fe_3O_4	60
Cr-Fe	23.1/76.9	51	20.9	28	$\text{FeCr}_2\text{O}_4/\text{Cr}_2\text{O}_3$	20.8/28.9
Cr	0/100	39	32.13	24	Cr_2O_3	36.8

^a Determined by XPS; ^b Calculated from nitrogen adsorption-desorption results; ^c Calculated from Scherrer formula at the (1 0 4) crystal plane of $(\text{Fe,Cr})_2\text{O}_3$. ^d calculated from Scherrer formula at the related phase in used catalysts.

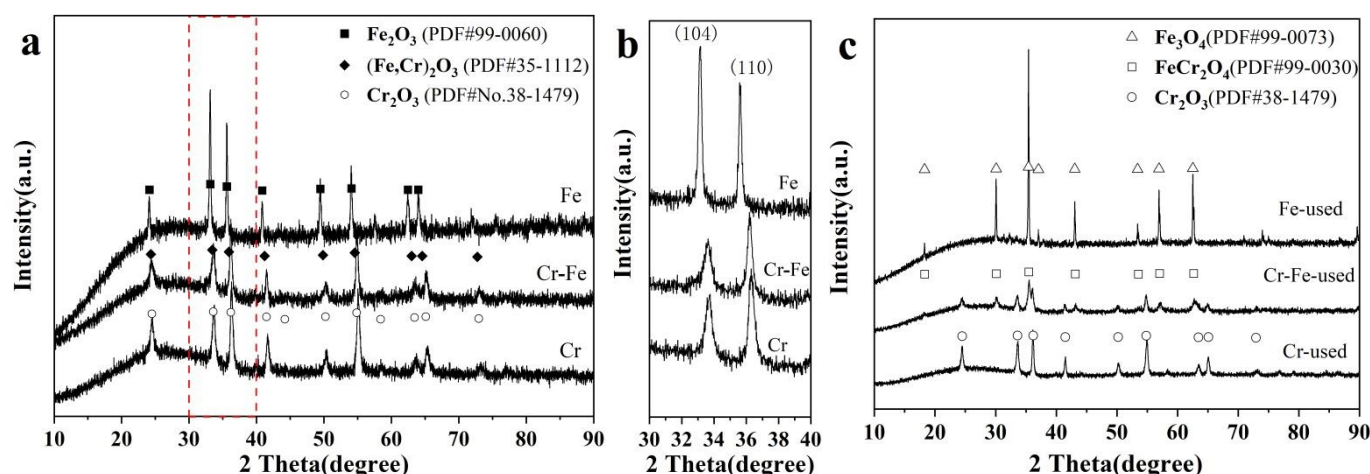


Fig. 3. (a) XRD patterns of fresh FeCrO_x catalysts, (b) The magnified portion of the curve in the 30-40° range in (a), (c) XRD patterns of used FeCrO_x catalysts.

In consideration of incomplete dissolution in ICP-OES tests and structural homogeneity for the Cr-Fe sample, the quantitative analysis of iron and chromium elements was calculated by XPS fitting results. As shown in Table 1, the surface atomic ratio of Fe to Cr in the Cr-Fe catalyst is 23.1:76.9, well consistent with the designed value, verifying the effectiveness of the two-step urea hydrolysis method. Furthermore, the pore structure and specific surface area of the fresh samples were characterized using N_2 physical adsorption experiments. The specific surface areas of the fresh Fe, Cr-Fe, and Cr samples are $13 \text{ m}^2/\text{g}$, $51 \text{ m}^2/\text{g}$, and 39

m²/g, respectively. The nitrogen adsorption and desorption isotherms of all catalysts exhibit type V curves, indicating weak interactions between the adsorbent and the adsorbate. The presence of hysteresis loops is caused by the inter-particle pores (Fig. S4). The BJH average pore diameter of fresh Cr-Fe sample was 20.9 nm, which is significantly smaller than those of the monometallic Fe (44.75 nm) and monometallic Cr (32.13 nm) samples. The particle size of all fresh samples was well consistent with the XRD results. Therefore, the Cr-Fe sample exhibits a higher specific surface area and a smaller particle size than those of the monometallic Fe and Cr samples, which may be beneficial for the adsorption and activation of reactant molecules.

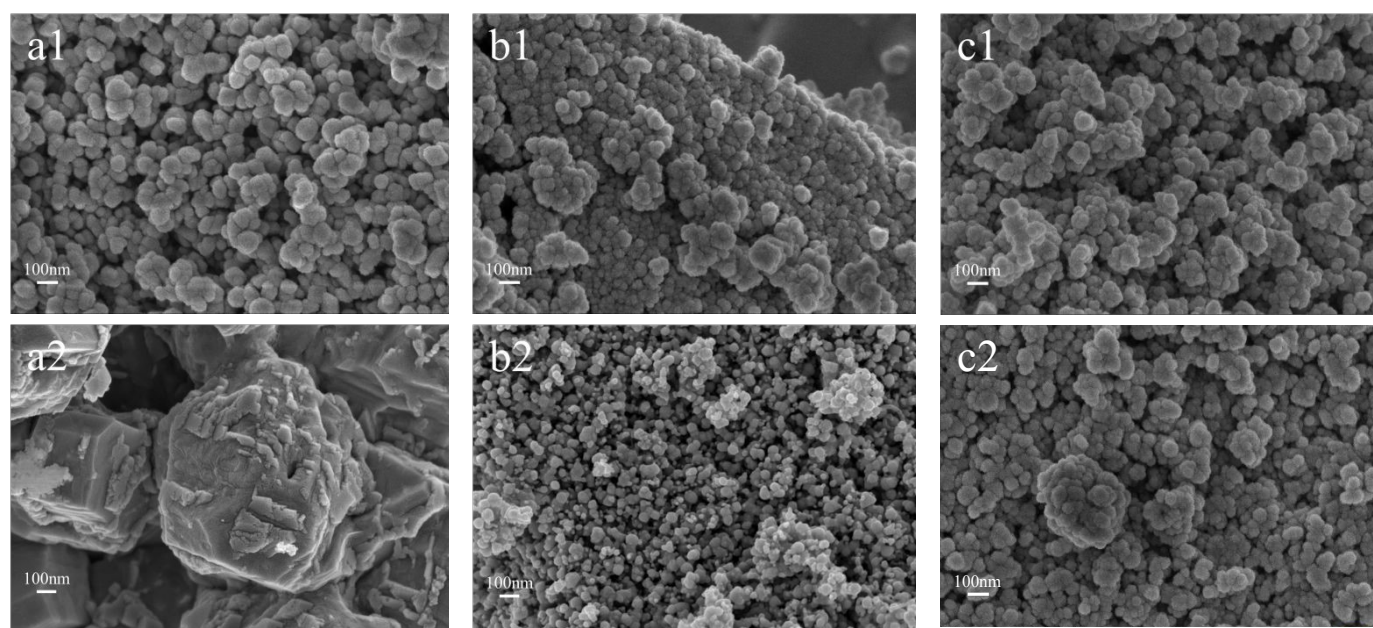


Fig. 4. SEM images of FeCrOx catalyst samples (1) before and (2) after the reaction: (a) Fe, (b) Cr-Fe, (c) Cr.

Fig. 4 shows the SEM images of the Fe, Cr-Fe, and Cr catalysts before and after the reaction. It can be seen that the morphology of the three fresh samples was quite similar, all approximately spherical and uniform in size, with secondary particle sizes ranging from several tens to a hundred nanometers, as shown in Fig. 4a1, b1, and c1. However, after the CO₂-ODHE reaction at 700 °C, there is a significant agglomeration and growth in particle size of the monometallic Fe sample (Fig. 4a2), with morphology changing from spherical to angular polygons because of the low melting point of iron oxide and high diffusion rate of iron ions during the transformation of Fe₂O₃ into Fe₃O₄^{34, 35}. In contrast, the spherical morphology of Cr and Cr-Fe samples can be well maintained without obvious aggregation after the CO₂-ODHE reaction. It further evident the good

ability of anti-sintering for the formation of FeCr_2O_4 .

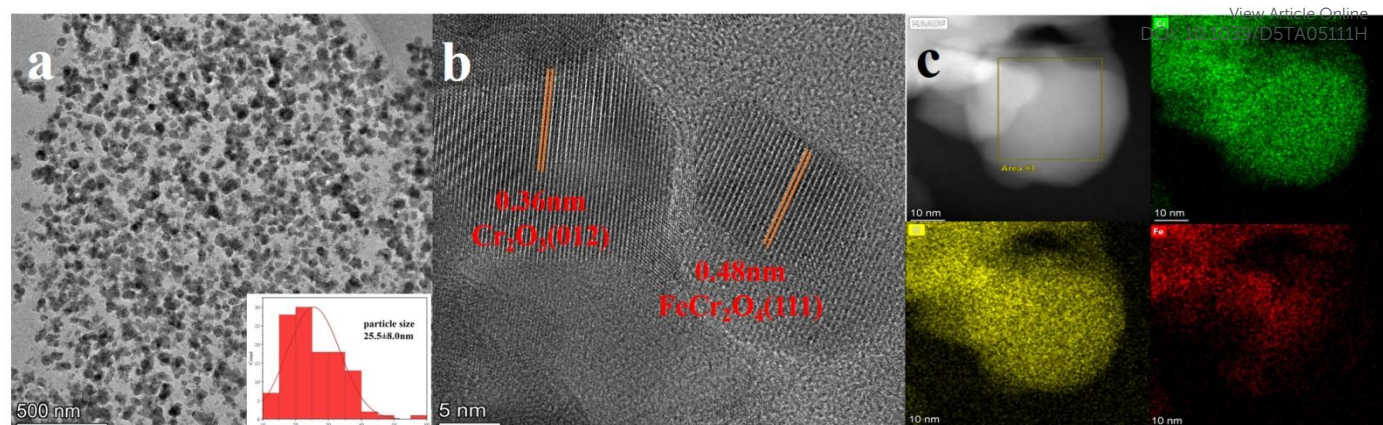


Fig. 5. (a) TEM (b) High-resolution TEM images and (c) elemental mapping images of the Cr-Fe-used catalyst

Meanwhile, the TEM and HRTEM characterizations further provided the detailed information about the morphology, size, and shape of the Cr-Fe-used sample under a microdomain view (Fig. 5). The TEM image in Fig. 5a displays that the Cr-Fe-used sample is composed of polyhedron-like nanoparticles with an average particle size of $\sim 25.5 \pm 8.0$ nm, in good agreement with XRD results. In the high-resolution TEM images, two distinct lattice fringes were clearly visible, in which the interplanar distances of 0.36 nm and 0.48 nm were attributed to the (012) plane of Cr_2O_3 and the (111) plane of FeCr_2O_4 , respectively. Taking the particle size of active site over 20 nm, an area about 70 nm^2 was chosen to conduct EDS mapping experiment (Fig. 5c) for the guarantee of data reliability. It indicated that the Cr and Fe elements were distributed uniformly in the component of FeCr_2O_4 in some areas, with isolated Cr element in other area from Cr_2O_3 . It further demonstrated that FeCr_2O_4 was stable after CO_2 -ODHE reaction.

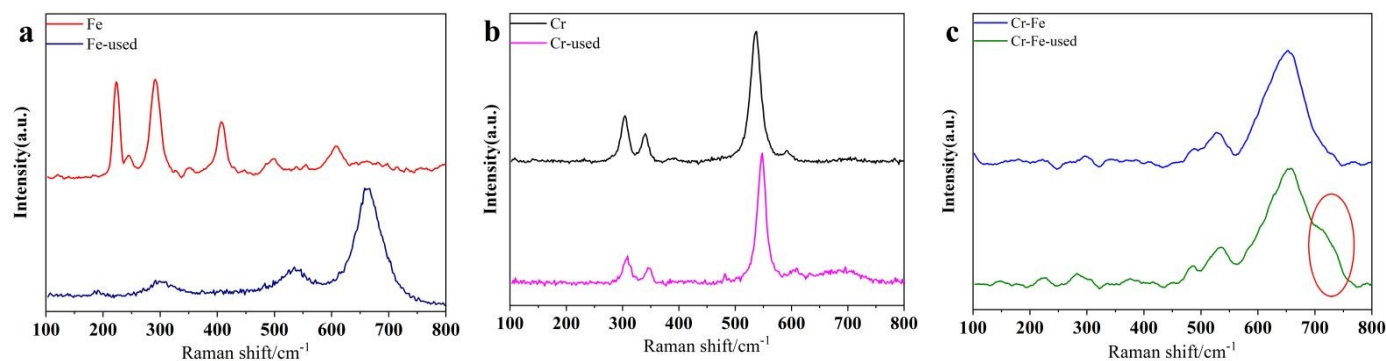
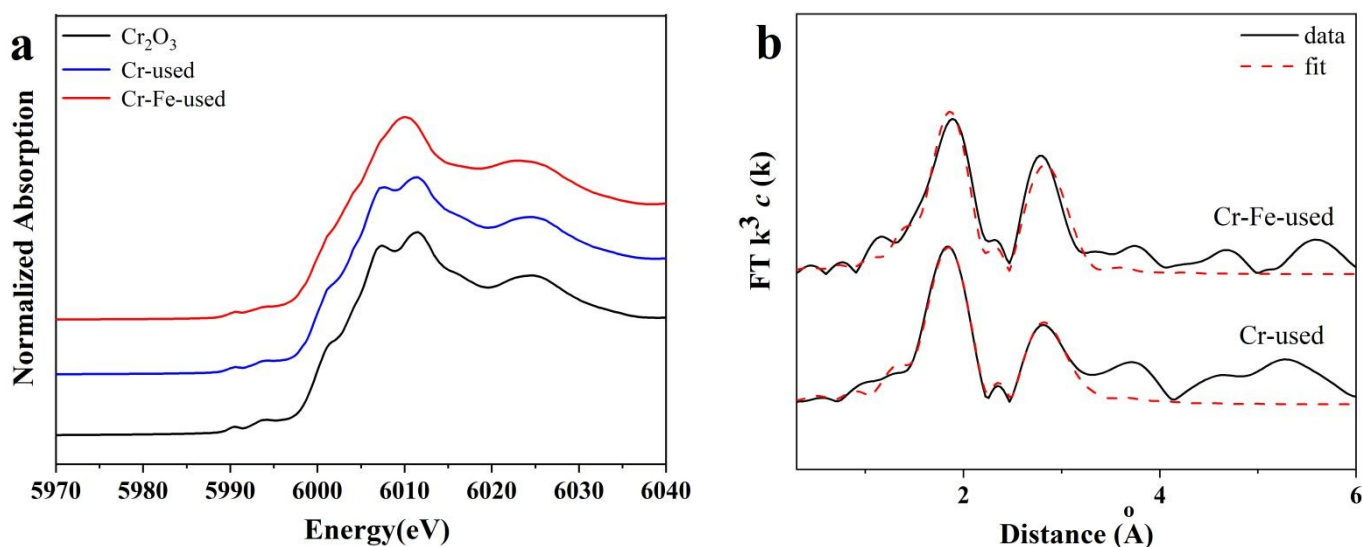


Fig. 6. Raman patterns of (a) Fe, (b) Cr, and (c) Cr-Fe catalysts before and after the reaction.

Fig. 6 presents the Raman spectra for the Fe, Cr, and Cr-Fe samples before and after the reaction to

provide fine surface structural information. The Raman spectrum of the fresh Fe sample displayed typical features of Fe_2O_3 , with notable peaks at 224, 245, 292, 407, 496, and 609 cm^{-1} , corresponding to the six vibrational modes ($\text{A}_{1\text{g}}(1)$, $\text{E}_{\text{g}}(1)$, $\text{E}_{\text{g}}(2)$, $\text{E}_{\text{g}}(3)$, $\text{E}_{\text{g}}(4)$, $\text{A}_{1\text{g}}(2)$)^{21, 36} in Fig. 6a. The fresh Cr sample exhibited characteristic Raman peaks of Cr_2O_3 , occurring at 304 cm^{-1} (E_{g}), 341 cm^{-1} (E_{g}), 537 cm^{-1} (A_{g}), and 592 cm^{-1} (E_{g})³⁶⁻³⁸ (Fig. 6b). For the Cr-Fe mixed sample, the most evident difference in the spectrum of the Cr-Fe mixed oxide compared to its parent binary oxides is the presence of a very strong band in the region of 560-700 cm^{-1} , which is completely absent in the monometallic oxides and is indicative of the characteristic peak of FeCrOx mixed oxide^{37, 39} (Fig. 6c). Previous studies have indicated that this strong band is associated with magnons, which represent collective excitations of electron spins and anisotropic magnetic interactions within the lattice framework^{36, 38, 40}. After the reaction, the Raman spectrum of the Fe-used sample shows significant changes with peaks at 299, 534, and 662 cm^{-1} , corresponding to Fe_3O_4 ^{37, 39}. In contrast, the Cr-used sample shows a blue shift in the characteristic vibrational peaks of Cr_2O_3 , indicating the decrease of oxygen vacancies on the catalyst surface after the reaction⁴¹. Notably, the peak positions of the Cr-Fe-used sample do not show a significant shift after CO_2 -ODHE reaction, however, a prominent shoulder appears at 695-750 cm^{-1} , confirming the presence of the spinel phase FeCr_2O_4 ^{21, 37, 39, 42} in the Cr-Fe-used sample.



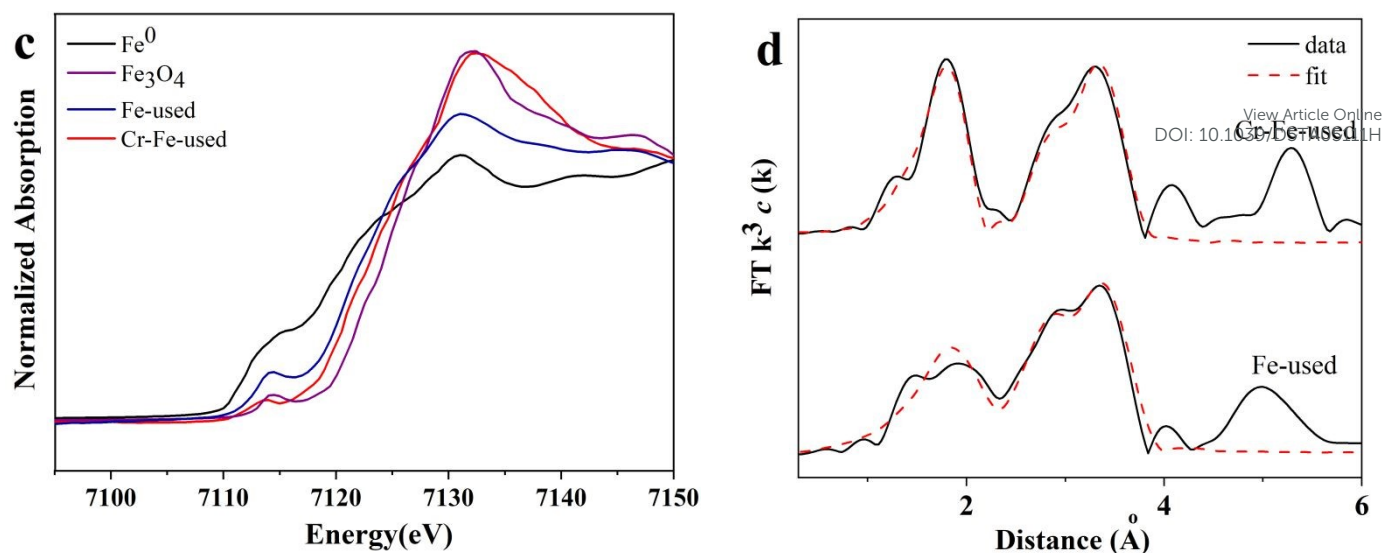


Fig. 7. Cr K-edge (a) XANES profiles, (b) EXAFS fitting results and Fe K-edge (c) XANES profiles, (d) EXAFS fitting results in R space of used FeCrOx catalysts.

The element-sensitive XAFS technique was used to determine the precise electronic and local coordination structures of the Fe and Cr species in used Fe, Cr-Fe, and Cr catalysts. The near-edge region (XANES) of the XAFS spectra provided electronic information about the metal atoms under investigation. The absorption edge energy, white line peak intensity, and pre-edge features are all related to the oxidation state of the metal. The XANES spectra of Cr-used and Cr-Fe-used samples in Fig. 7a indicated that the average oxidation state of Cr element in Cr-containing samples was +3, without further being reduced into metallic Cr state during the reaction. According to XRD and HRTEM results, the Cr species was in the formation of Cr_2O_3 and FeCr_2O_4 in Cr-Fe-used sample. There was a strong Cr-O shell at ~ 2.0 Å with a coordination number of 6.4 ± 0.7 and 6.7 ± 0.6 for Cr-used and Cr-Fe-used samples, respectively. For the second shell, a coordination structure of Cr-O-Cr at ~ 2.95 Å can be fitted for Cr-used and Cr-Fe-used samples, in which the coordination number of Cr-O-Cr/Fe shell for Cr-used (~ 2.5) and Cr-Fe-used (~ 4.5) samples was obviously different (Fig. 7b and Table S3). It further demonstrated that FeCr_2O_4 possessed a different coordination structure with Cr_2O_3 .

Furthermore, the Fe K-edge (7112 eV) XAFS measurements of the Fe-used and Cr-Fe-used catalysts were also conducted in Fig. 7c, 7d and Table S4. The edge jump energy of Fe-used and Cr-Fe-used were between Fe-foil and Fe_3O_4 . The average oxidation state of iron for Fe-used and Cr-Fe-used was +2.2 and +2.6,



respectively, calculated by linear combination fitting results in Fig. S5 and Table S4. The EXAFS spectrum of Fe-used and Cr-Fe-used samples in Fig. 7d exhibited the coordination structure of Fe species. For the Fe-used, the Fe-O ($R \approx 2.0$ Å, $CN \approx 3.9$), Fe-O-Fe¹ ($R \approx 2.97$ Å, $CN \approx 3.9$) and Fe-O-Fe² ($R \approx 3.49$ Å, $CN \approx 11.6$) shells were acquired, which were assigned to the typical Fe₃O₄ structure. In addition, a tiny Fe-Fe ($R \approx 2.52$ Å, $CN \approx 1.2$) was necessary for Fe-used using Fe-foil model, which was well consistent with the lower average oxidation state over iron species. For Cr-Fe-used sample, the coordination number of Fe-O shell at $R \approx 1.94$ Å increased to 5.4. Fe-O-Fe¹ ($R \approx 2.92$ Å, $CN \approx 2.4$) and Fe-O-Cr ($R \approx 3.47$ Å, $CN \approx 12.1$) were acquired. According to XAFS results, it can be seen that there were more oxygen atoms surrounding Fe species in FeCr₂O₄, which may be benefit for the elimination of deposition coke. Based on the combined results of XRD, HRTEM and XAFS results, we can confirm that the main active sites in Fe, Cr-Fe and Cr samples are Fe₃O₄, FeCr₂O₄ and Cr₂O₃, respectively.

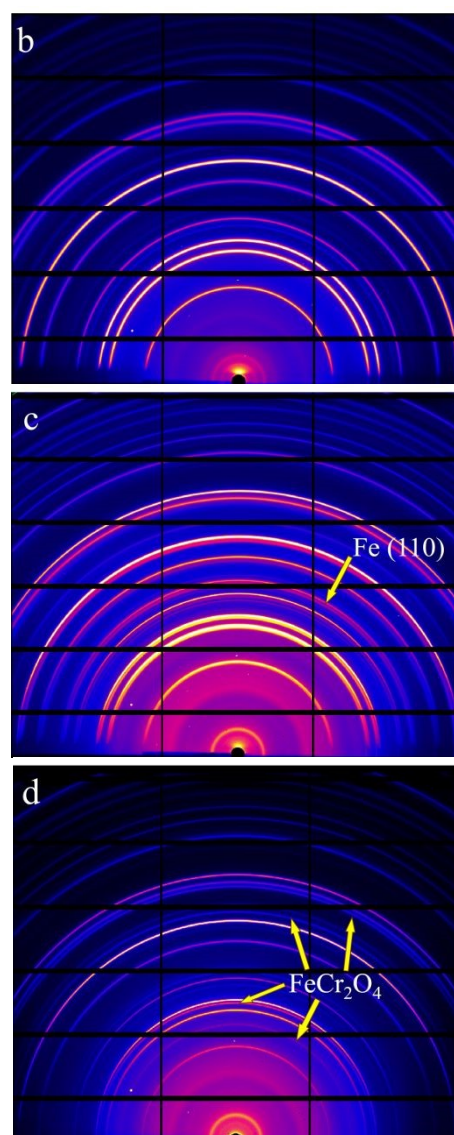
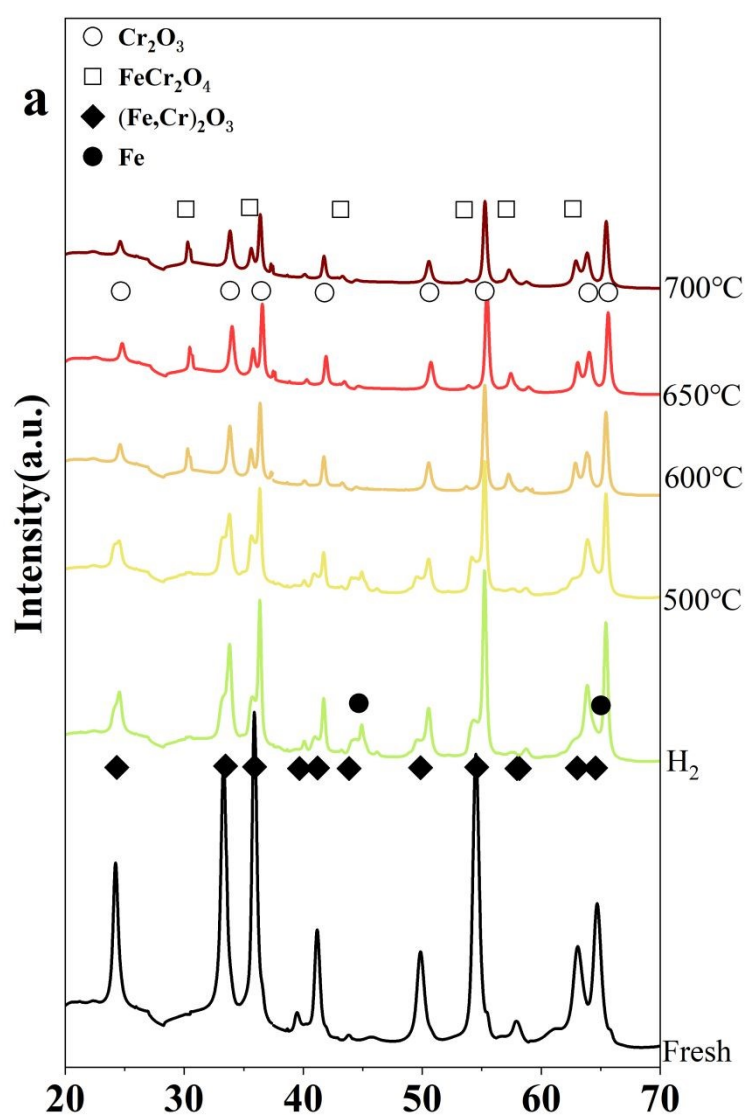


Fig. 8. In-situ SR-XRD (a) patterns of Cr-Fe catalyst during CO₂-ODHE reaction and 2D images of (b) fresh (c) 450 °C in the 50% H₂/Ar (d) 650 °C in the reaction gases (CO₂/C₂H₆/Ar = 10/10/20 mL/min)

Additionally, the phase transformation process of the Cr-Fe catalyst from hydrogenation pretreatment to CO₂-ODHE reaction was in-situ monitored by synchrotron radiation XRD (SR-XRD). The 2D-XRD pattern exhibits distinct concentric rings, with non-uniform intensity distribution of the diffraction rings observed within the azimuthal angle range of 0°-180°, indicating a preferred orientation of the crystals along specific crystal planes (Fig. 8). Through radial integration, the 2D image was converted into a 1D diffraction pattern. As expected, the fresh sample exhibited the clearly visible diffraction rings, ordered from the center outward, correspond to the diffraction peaks at 24.3, 33.5, 35.9, 41.2, 49.8, and 54.6°, which are indexed to the (012), (104), (110), (113), (024), and (116) crystal planes of the (Fe,Cr)₂O₃ (JCPDS No.35-1112) solid solution at room temperature (Fig. 8a,b), respectively. After the reduction, the (Fe,Cr)₂O₃ solid solution was gradually reduced to Fe⁰ (JCPDS No.06-0696) with the appearance of an additional diffraction ring appears at 44.5° (indicated by an arrow in Fig 8c). The diffraction peaks at 24.5, 33.6, and 36.2° of Cr₂O₃ (JCPDS No.38-1479) became distinctly visible. Upon switching to the reaction atmosphere, the disappearance of Fe⁰ diffraction peak at 44.5° indicates that Fe⁰ cannot remain stable under the reaction conditions in the presence of the oxidizing CO₂ atmosphere. With the absence of diffraction peaks at 33.4, 41.2, and 49.8° signified the complete disappearance of the (Fe, Cr)₂O₃ solid solution phase, the new diffraction peaks at 30.1, 35.5, and 57.1° just appeared, corresponding to the diffraction ring observed at the position indicated by the arrow in Fig. 8d, indicating the formation of FeCr₂O₄ under the reaction condition. Furthermore, with the development of reaction, the FeCr₂O₄ component was generated and maintained for the whole reaction.

Moreover, when the pretreatment gas was altered to air and inert gas (Ar) instead of the reducing hydrogen atmosphere (Fig. S6), it was observed that a reducing pretreatment atmosphere slightly favored the conversion of ethane than the others at lower temperatures, suggesting that the reductive pretreatment atmosphere promotes the phase transformation process, thereby effectively shortening the induction period



for the generation of active phase. Notably, even when oxidative (air) or inert (Ar) atmospheres are used instead of H_2 pretreatment, the $FeCr_2O_4$ phase remains stable after the reaction (Fig. S7), which may be due to the inevitable generation of reductive H_2 in the CO_2 -ODHE reaction. Therefore, the in-situ XRD experiments further confirmed the generation of the spinel-structured $FeCr_2O_4$ during the CO_2 -ODHE reaction, which had previously been identified as the active phase for this reaction through TEM and Raman characterizations.

3.3. Catalyst Reaction Mechanism

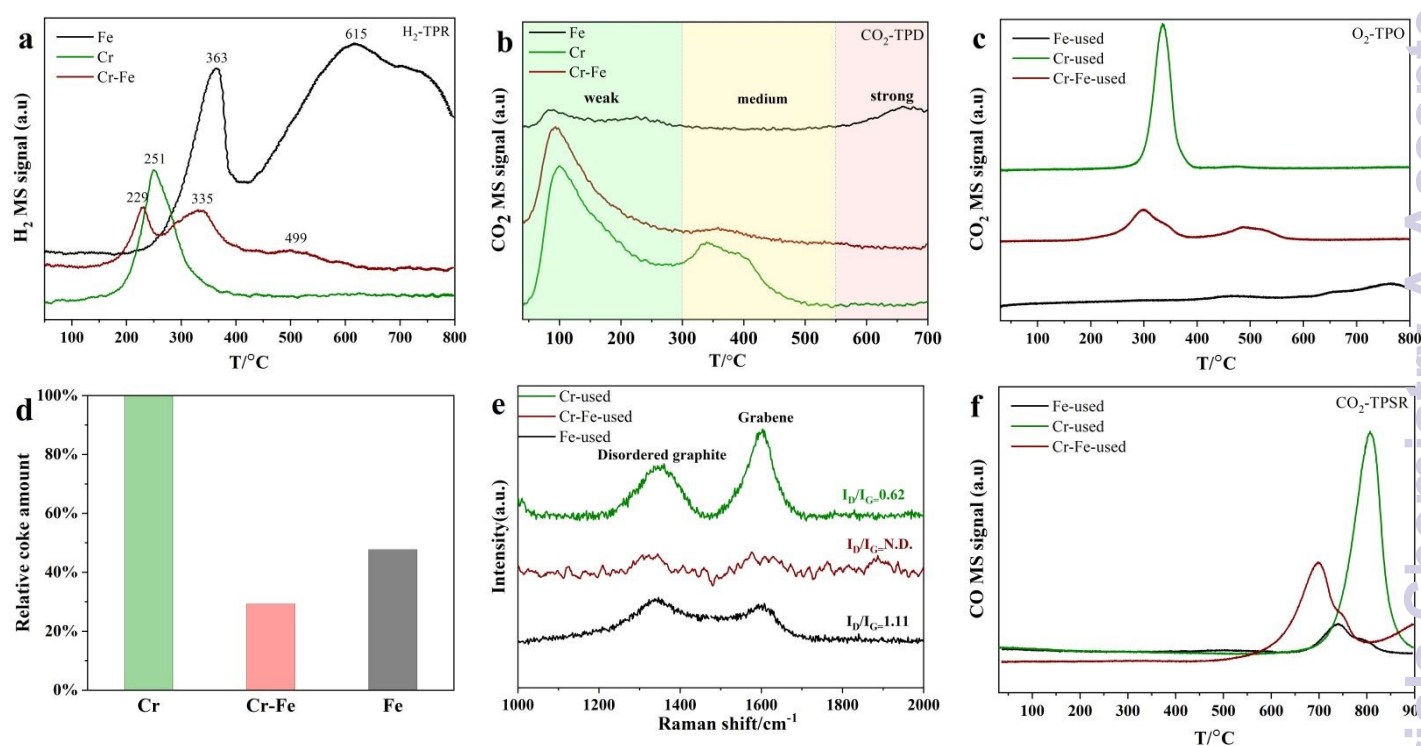


Fig. 9. (a) H_2 -TPR and of fresh $FeCrO_x$ samples (b) CO_2 -TPD of $FeCrO_x$ samples, (c) O_2 -TPO and (f) CO_2 -TPSR of used $FeCrO_x$ samples, (d) the estimated relative coke deposition on the catalyst from (c), and (e) Raman spectra of used $FeCrO_x$ samples in the wavenumber range of 1000-2000 cm^{-1} .

To further investigate the reducibility and metal-oxide interaction of the $FeCrO_x$ catalysts, H_2 -TPR characterization was conducted on the Fe, Cr, and Cr-Fe samples. As shown in Fig. 9a, the fresh Fe sample exhibits two peaks at 363 °C and after 400 °C (with a peak center at 615 °C). The first peak was assigned to the reduction of Fe_2O_3 to Fe_3O_4 , while the latter peak (after 400 °C) can be attributed to the reduction of Fe_3O_4

to Fe^{2+} and Fe^0 ⁴³⁻⁴⁵. For the fresh Cr sample, only a reduction peak at 251 °C can be observed, originating from the reduction of surface Cr^{6+} species to Cr^{3+} , which are reported to coexist on the catalyst surface under oxidizing conditions^{12, 14} and are reduced at relatively low temperatures (200-300 °C)^{21, 35, 46}. For the fresh Cr-Fe samples, the reduction peaks at 229, 335 and 499 °C were attributed to the reduction of surface Cr^{6+} species, Fe^{3+} to Fe^{2+} and Fe^0 , which were much lower than those in monometallic Fe and Cr samples. It indicated that the formation of $(\text{Fe,Cr})_2\text{O}_3$ solid solution can improve the reducibility of Fe and Cr species.

Table 2. CO_2 desorption peak area for FeCrO_x catalysts^a

Sample	$S_{\text{weak}} / S_{\text{medium}} / S_{\text{strong}} (\times 10^{-7})$
Fe	2.6/0/0.6
Cr-Fe	12.5/0.3/0
Cr	18.5/3.2/0

^a Estimated by CO_2 -TPD.

We used CO_2 -TPD experiments to characterize the CO_2 adsorption capacity of active site properties for different catalysts. The basicity of catalysts, which can be correlated to their CO_2 desorption temperature, is typically categorized as follows: weak (< 300 °C), medium (300-500 °C) and strong (> 500 °C). Prior to TPD, the catalyst sample was processed with 5% H_2/Ar (50 $\text{mL} \cdot \text{min}^{-1}$) at 450 °C for 90 min. As shown in Fig. 9b and Table 2, the Fe sample exhibits tiny CO_2 desorption peaks at 90 °C and 660 °C, indicating the weak CO_2 adsorption capacity of Fe_3O_4 . It also was agreement with the catalytic performance, in which the Fe catalyst exhibited low CO_2 conversion. For the Cr catalyst, the CO_2 desorption peaks occurred primarily at 100 °C and 338 °C, which are assigned to weak and medium basic sites, respectively. This demonstrates that Cr_2O_3 is beneficial for adsorbing CO_2 to participate in the CO_2 -ODHE reaction, thereby contributing to the higher CO_2 conversion over the Cr catalyst (Fig. 1b). However, for Cr-Fe sample, only a visual and strong CO_2 adsorption peak at ~100 °C can be detected, suggesting weak basicity on FeCr_2O_4 , in which the weak basicity may be a key point in higher C_2H_4 yield for Cr-Fe sample. The presence of weak basic sites improved selectivity to alkene and reduced coke formation⁴⁷. In contrast, the strong basic sites favor the side reactions, such as reforming and cracking reactions, leading to significant coke deposition and reduced reaction activity¹⁴. The

He-TPSR experiments confirmed that both the Cr_2O_3 and FeCr_2O_4 catalysts contain certain active oxygen species capable of reacting with deposited coke, exhibiting similar light-off temperatures (Fig. S8). However, CO_2 molecules adsorbed on the weak and medium basic sites should be relatively active and can readily participate in reactions, especially the weak basic sites⁴⁸. Therefore, the Cr-Fe sample exhibits superior CO_2 adsorption and activation capabilities, attributable to its weak basic sites. This property facilitates the gasification of carbon deposits, thereby effectively mitigating coke accumulation. Furthermore, the O_2 -TPO experiment also certified the lowest amount of coke deposition in Cr-Fe-used sample (Fig. 9c). Generally, the carbon species with a lower peak temperature shows a higher activity and can be easily removed^{18, 49}. For Cr-used sample, a strong CO_2 peak at 330 °C can be observed, which was well consistent with the low carbon balance in Fig. 2b. Furthermore, two peaks at ~300 °C and 500 °C was acquired in Cr-Fe-used sample, which can be attributed to the oxidation of coke on Cr_2O_3 and FeCr_2O_4 respectively, with much less coke deposition on FeCr_2O_4 . For Fe-used samples, the amount of coke deposited is small because of low activity in CO_2 -ODHE reaction. By integrating the CO_2 peaks from the mass spectrometry data and normalizing against the ethane conversion rate, we compared the relative coke amounts per unit mass of used catalysts (Fig. 9d). The monometallic Cr-used sample exhibited the highest quantity of coke deposition, under the lower activity than that of Cr-Fe-used catalysts, due to the medium basicity. The Raman spectra of used samples (Fig. 9e) also showed that the Fe-used and Cr-used samples exhibited prominent D bands (disorder-induced, ~1430 cm^{-1}) and G bands (in-plane vibrations, ~1610 cm^{-1}) associated with coke deposition⁵⁰. However, these tiny peaks at ~1430 cm^{-1} and ~1610 cm^{-1} in the Cr-Fe-used sample made it impossible to evaluate the degree of carbon graphitization using the ID/IG intensity ratio value. In addition, the conversion of CO_2 plays a key role in the elimination of coke deposition in CO_2 -ODHE reaction through the oxidation of coke by CO_2 molecule. In Fig. 9f, it can be seen that CO_2 can react with surface deposited coke to release CO at 550 °C in Cr-Fe-used sample, continuing until 800 °C. The results indicate that FeCr_2O_4 can effectively activate CO_2 molecules, enabling the Boudouard reaction ($\text{C} + \text{CO}_2 \rightarrow 2\text{CO}$) with deposited coke even at relatively low temperatures. Moreover,



CO₂ in the reaction stream continuously reacts with carbon deposits across the entire temperature range of the CO₂-ODHE reaction (500 -700 °C), thereby contributing to the improvement of catalytic performance. In contrast, significant CO release for the monometallic catalyst samples was observed only at 700 °C. Despite the continuous oxygen supply from CO₂ before this temperature, it could not react with the surface coke on the catalysts, aligning with the observed reaction activity. Based on these results, it can be concluded that the FeCr₂O₄ phase effectively adsorbs and activates CO₂, thereby facilitating coke removal and promoting the CO₂-ODHE reaction.

Additionally, the Cr-Fe sample that lost activity after the stability test (650°C, >12h) was regenerated by calcining in air at 600°C to remove coke (Fig.S9a). Subsequent stability tests showed the initial conversion rates and yields were restored, but revealed recurring deactivation patterns with continued reaction, indicating that the gradual accumulation of coke is the primary cause of FeCrO_x catalyst deactivation. Significantly, CO₂-TPSR results demonstrate FeCr₂O₄ able to activate CO₂ for low-temperature carbon gasification. To validate this in-situ regeneration strategy, we performed cyclic CO₂ treatments on deactivated catalysts (Fig. S9b). Each regeneration cycle substantially restored ethane conversion (>95% recovery) while maintaining ethylene yield above 15% throughout repeated testing. These findings collectively establish continuous CO₂ purging as a promising operational strategy to mitigate coke-induced deactivation during reaction.

4. Conclusions

In summary, nano iron oxide, chromium oxide, and FeCr bimetallic oxides were synthesized using a two-step urea precipitation method and subjected to CO₂ oxidative dehydrogenation of ethane catalytic tests. The Cr-Fe sample exhibited significantly higher activity compared to the monometallic samples with the conversion of ethane and CO₂ approached 35% and 27% at 650 °C, respectively. And the formation rate of C₂H₄ was about 13.4 μmol g⁻¹ cat s⁻¹ with the C₂H₄ yield remained at 18% for 300 min. Through XRD, Raman, SEM and XAFS characterization, it was found that the monometallic Fe sample transformed from Fe₂O₃ to Fe₃O₄ during the reaction and underwent sintering. Although the monometallic Cr sample did not show

significant phase changes, it tends to deactivate due to substantial coke formation. In contrast, the bimetallic Cr-Fe sample formed a solid solution oxide of $(\text{Fe,Cr})_2\text{O}_3$, effectively reducing catalyst grain size and resisting sintering. The in-situ formation and stable spinel structure of FeCr_2O_4 during the reaction, which were characterized by synchrotron radiation-based in-situ XRD, confirm that FeCr_2O_4 is the active phase for the CO_2 -ODHE reaction. Moreover, the Cr-Fe sample with weak basic sites exhibits superior CO_2 adsorption and activation capabilities. According to O_2 -TPO and CO_2 -TPSR of the used samples, the FeCr_2O_4 enabling the combustion of coke deposited on the catalyst surface at lower temperatures, thus significantly enhancing the reaction activity and regeneration stability. Our work may provide theoretical guidance for the industrial application of non-noble metal catalysts in CO_2 oxidative dehydrogenation of ethane.

Acknowledgements

This work was supported by “Photon Science Research Center for Carbon Dioxide”, “Project of the National Natural Science Foundation of China” (22332003, 12505386), Science and Technology Innovation Plan of Shanghai Science and Technology Commission (23YF1453700), “Shanghai Municipal Science and Technology Commission” (23JC1403300), “2025 Research Equipment Project of the Special Fund for Improving Research Conditions in Central-Level Scientific Institutions, Chinese Academy of Sciences” and “Shanghai Municipal Science and Technology Major Project”. We appreciate the assistance of TILON Group Technology Limited (Division of China) in characterization of catalysts. Additionally, the User Experiment Assist System (<https://cstr.cn/31124.02.SSRF.LAB>), 14W1, 02U2, 13SSW, 17B, and 16U1 beamline of SSRF provided support for data collecting for this work.

References

- (1) de Oliveira, J. F. S.; Volanti, D. P.; Bueno, J. M. C.; Ferreira, A. P. Effect of CO_2 in the oxidative dehydrogenation reaction of propane over Cr/ZrO_2 catalysts. *Applied Catalysis A: General* **2018**, 558, 55-66. DOI: 10.1016/j.apcata.2018.03.020.
- (2) Yang, G.-Q.; Wang, H.; Gong, T.; Song, Y.-H.; Feng, H.; Ge, H.-Q.; Ge, H.-b.; Liu, Z.-T.; Liu, Z.-W. Understanding the active-site nature of vanadia-based catalysts for oxidative dehydrogenation of ethylbenzene with CO_2 via atomic layer deposited VO_x on $\gamma\text{-Al}_2\text{O}_3$. *Journal of Catalysis* **2019**, 380, 195-203. DOI: 10.1016/j.jcat.2019.10.009.
- (3) Wang, L.-C.; Zhang, Y.; Xu, J.; Diao, W.; Karakalos, S.; Liu, B.; Song, X.; Wu, W.; He, T.; Ding, D. Non-oxidative dehydrogenation of ethane to ethylene over ZSM-5 zeolite supported iron catalysts. *Applied Catalysis B: Environmental* **2019**, 256,

117816. DOI: 10.1016/j.apcatb.2019.117816.
- (4) Zhang, Y.; Chen, M.; Wang, W.; Zhang, Y. A stable Pt modified cobalt tungstate catalyst for CO₂-assisted oxidative dehydrogenation of ethane. *Catalysis Science & Technology* **2024**, *14* (14), 3924-3935. DOI: 10.1039/d4cy00399c. View Article Online DOI: 10.1039/D5TA05111H
- (5) Gomez, E.; Yan, B.; Kattel, S.; Chen, J. G. Carbon dioxide reduction in tandem with light-alkane dehydrogenation. *Nature Reviews Chemistry* **2019**, *3* (11), 638-649. DOI: 10.1038/s41570-019-0128-9.
- (6) Liu, P.; Zhang, L.; Li, M.; Sun, N.; Wei, W. Recent progress in Cr-based catalysts for oxidative dehydrogenation of light alkanes by employing CO₂ as a soft oxidant. *Clean Energy* **2021**, *5* (4), 623-633. DOI: 10.1093/ce/zkab036.
- (7) Bugrova, T. A.; Dutov, V. V.; Svetlichnyi, V. A.; Cortés Corberán, V.; Mamontov, G. V. Oxidative dehydrogenation of ethane with CO₂ over CrO_x catalysts supported on Al₂O₃, ZrO₂, CeO₂ and Ce_xZr_{1-x}O₂. *Catalysis Today* **2019**, *333*, 71-80. DOI: 10.1016/j.cattod.2018.04.047.
- (8) Gambo, Y.; Adamu, S.; Tanimu, G.; Abdullahi, I. M.; Lucky, R. A.; Ba-Shammakh, M. S.; Hossain, M. M. CO₂-mediated oxidative dehydrogenation of light alkanes to olefins: Advances and perspectives in catalyst design and process improvement. *Applied Catalysis A: General* **2021**, *623*.118273 DOI: 10.1016/j.apcata.2021.118273.
- (9) Maroño, M.; Ruiz, E.; Sánchez, J. M.; Martos, C.; Dufour, J.; Ruiz, A. Performance of Fe–Cr based WGS catalysts prepared by co-precipitation and oxi-precipitation methods. *International Journal of Hydrogen Energy* **2009**, *34* (21), 8921-8928. DOI: 10.1016/j.ijhydene.2009.08.068.
- (10) Porosoff, M. D.; Myint, M. N. Z.; Kattel, S.; Xie, Z.; Gomez, E.; Liu, P.; Chen, J. G. Identifying Different Types of Catalysts for CO₂ Reduction by Ethane through Dry Reforming and Oxidative Dehydrogenation. *Angewandte Chemie International Edition* **2015**, *54* (51), 15501-15505. DOI: 10.1002/anie.201508128.
- (11) Cheng, Y.; Gong, H.; Miao, C.; Hua, W.; Yue, Y.; Gao, Z. Ga₂O₃/HSSZ-13 for dehydrogenation of ethane: Effect of pore geometry of support. *Catalysis Communications* **2015**, *71*, 42-45. DOI: 10.1016/j.catcom.2015.08.015.
- (12) Wang, S-B, K. M., T. Hayakawa, S. Hamakawa, K. Suzuki. Dehydrogenation of ethane with carbon dioxide oversupported chromium oxide catalysts. *Applied Catalysis A: General* **2000**, *196*, 1-8.
- (13) Koirala, R.; Safonova, O. V.; Pratsinis, S. E.; Baiker, A. Effect of cobalt loading on structure and catalytic behavior of CoO_x/SiO₂ in CO₂-assisted dehydrogenation of ethane. *Applied Catalysis A: General* **2018**, *552*, 77-85. DOI: 10.1016/j.apcata.2017.12.025.
- (14) Deng, S.; Li, H.; Li, S.; Zhang, Y. Activity and characterization of modified Cr₂O₃/ZrO₂ nano-composite catalysts for oxidative dehydrogenation of ethane to ethylene with CO₂. *Journal of Molecular Catalysis A: Chemical* **2007**, *268* (1-2), 169-175. DOI: 10.1016/j.molcata.2006.12.033.
- (15) Numan, M.; Eom, E.; Li, A.; Mazur, M.; Cha, H. W.; Ham, H. C.; Jo, C.; Park, S.-E. Oxidative Dehydrogenation of Ethane with CO₂ as a Soft Oxidant over a PtCe Bimetallic Catalyst. *ACS Catalysis* **2021**, *11* (15), 9221-9232. DOI: 10.1021/acscatal.1c01156.
- (16) Mimura, N.; Takahara, I.; Inaba, M.; Okamoto, M.; Murata, K. High-performance Cr/H-ZSM-5 catalysts for oxidative dehydrogenation of ethane to ethylene with CO₂ as an oxidant. *Catalysis Communications* **2002**, *3* (6), 257-262. DOI: 10.1016/s1566-7367(02)00117-6.
- (17) Numan, M.; Kim, T.; Jo, C.; Park, S.-E. Ethane Dehydrogenation with CO₂ as a soft oxidant over a Cr-TUD-1 catalyst. *Journal of CO₂ Utilization* **2020**, *39*, 101184. DOI: 10.1016/j.jcou.2020.101184.
- (18) Yan, B.; Yao, S.; Kattel, S.; Wu, Q.; Xie, Z.; Gomez, E.; Liu, P.; Su, D.; Chen, J. G. Active sites for tandem reactions of CO₂ reduction and ethane dehydrogenation. *Proc Natl Acad Sci USA* **2018**, *115* (33), 8278-8283. DOI: 10.1073/pnas.1806950115.
- (19) Deng S, Li, S-G, Li, H-Q, and Zhang Y. Oxidative dehydrogenation of ethane to ethylene with CO₂ over Fe-CrZrO₂ catalysts. *Industrial & Engineering Chemistry Research* **2009**, *48*, 7561–7566. DOI: 10.1021/ie9007387
- (20) Kocovski, V.; Pilania, G.; Uberuaga, B. P. High-throughput investigation of the formation of double spinels. *Journal of Materials Chemistry A* **2020**, *8* (48), 25756-25767. DOI: 10.1039/d0ta09200b.
- (21) Bhandari, S.; Khatun, R.; Khan, T. S.; Khurana, D.; Poddar, M. K.; Shukla, A.; Prasad, V. V. D. N.; Bal, R. Preparation of a nanostructured iron chromite spinel in the pure form and its catalytic activity for the selective oxidation of benzene to phenol: experimental and DFT studies. *Green Chemistry* **2022**, *24* (23), 9303-9314. DOI: 10.1039/d2gc02335k.
- (22) Mishanin, I. I.; Bogdan, V. I. In situ CO₂ reactivation of FeCrO/C catalyst in the oxidative dehydrogenation of ethane to ethylene. *Mendeleviev Communications* **2020**, *30* (3), 359-361. DOI: 10.1016/j.mencom.2020.05.033.
- (23) Mishanin, I. I.; Bogdan, T. V.; Koklin, A. E.; Bogdan, V. I. Design of highly selective heterogeneous catalyst for CO₂-mediated

- ethane oxidative dehydrogenation based on nonoxidative catalysis in stainless-steel reactor. *Chemical Engineering Journal* **2022**, 446, 137184. DOI: 10.1016/j.cej.2022.137184.
- (24) Mishanin, I. I.; Bogdan, T. V.; Smirnov, A. V.; Chernavskii, P. A.; Kuznetsova, N. N.; Bogdan, V. I. Formation of active phases of Fe/C, Cr/C and Fe–Cr/C catalysts in oxidative dehydrogenation of ethane. *Mendelev Communications* **2023**, 33 (3), 422–424. DOI: 10.1016/j.mencom.2023.04.039.
- (25) Kim, O. A.; Bogdan, T. V.; Koklin, A. E.; Bogdan, V. I. Interaction of Carbon Dioxide with Hydrogen on Supported Fe, Cr-Containing Catalysts. *Russian Journal of Physical Chemistry B* **2023**, 16 (7), 1218–1220. DOI: 10.1134/s1990793122070107.
- (26) Bogdan, T. V.; Koklin, A. E.; Mishanin, I. I.; Chernavsky, P. A.; Pankratov, D. A.; Kim, O.-S. A.; Bogdan, V. CO₂ Hydrogenation on Carbides Formed in situ on Carbon-Supported Iron-Based Catalysts in High-Density Supercritical Medium. *ChemPlusChem* **2024**, 89, e202400327. DOI: 10.1002/cplu.202400327.
- (27) Ravel, B.; Newville, M. ATHENA, ARTEMIS, HEPHAESTUS: data analysis for X-ray absorption spectroscopy using IFEFFIT. *Journal of Synchrotron Radiation* **2005**, 12 (4), 537–541. DOI: 10.1107/s0909049505012719.
- (28) Cancino-Trejo, F.; Santes, V.; Cardenas, J. A. A.; Gallardo, M.; Maldonado, Y. G.; Miranda A, L.; Valdes, O.; de los Reyes, J. A.; Santolalla-Vargas, C. E. Active Ni and Fe species on catalysts Ni/Al₂O₃ and NiFe/Al₂O₃ for the oxidative dehydrogenation (ODH) of ethane to ethylene assisted by CO₂. *Chemical Engineering Journal Advances* **2022**, 12, 100404. DOI: 10.1016/j.cej.2022.100404.
- (29) Liu, P.; Zhang, L.; Wang, X.; Du, M.; Hao, Y.; Li, L.; Chen, X.; Sun, N.; Wei, W. Preparation, Structure-Performance Relationship, and Reaction Network of ZnZSM-5 for Oxidative Dehydrogenation of Ethane with CO₂. *Chemistry* **2023**, 29 (22), e202203960. DOI: 10.1002/chem.202203960 From NLM PubMed-not-MEDLINE.
- (30) Yao, S.; Yan, B.; Jiang, Z.; Liu, Z.; Wu, Q.; Lee, J. H.; Chen, J. G. Combining CO₂ Reduction with Ethane Oxidative Dehydrogenation by Oxygen-Modification of Molybdenum Carbide. *ACS Catalysis* **2018**, 8 (6), 5374–5381. DOI: 10.1021/acscatal.8b00541.
- (31) Shannon, R. D. Revised effective ionic radii and systematic studies of interatomic distances in halides and chalcogenides. *Acta Crystallographica Section A* **1976**, 32, 751–767. DOI: 10.1107/s0567739476001551.
- (32) Montero-Cabrera, M. E.; Fuentes-Cobas, L. E.; Macías-Ríos, E.; Fuentes-Montero, M. E. Application of x-ray absorption fine structure (XAFS) to local-order analysis in Fe-Cr maghemite-like materials. *AIP Conf. Proc.* **2015**, 1671, 020008. DOI: 10.1063/1.4927185.
- (33) García-Vázquez, M.; Wang, K.; González-Carballo, J. M.; Brown, D.; Landon, P.; Tooze, R.; García-García, F. R. Iron and chromium-based oxides for residual methane abatement under realistic conditions: A study on sulfur dioxide poisoning and steam-induced inhibition. *Applied Catalysis B: Environmental* **2020**, 277, 119139. DOI: 10.1016/j.apcatb.2020.119139.
- (34) Chinchén, G. C.; Logan, R. H.; Spencer, M. S. Water-gas shift reaction over an iron oxide/chromium oxide catalyst. *Applied Catalysis* **1984**, 12 (1), 89–96. DOI: 10.1016/s0166-9834(00)81506-7.
- (35) Meshkani, F.; Rezaei, M.; Jafarbegloo, M. Preparation of nanocrystalline Fe₂O₃–Cr₂O₃–CuO powder by a modified urea hydrolysis method: A highly active and stable catalyst for high temperature water gas shift reaction. *Materials Research Bulletin* **2015**, 64, 418–424. DOI: 10.1016/j.materresbull.2014.12.038.
- (36) M.I. Baraton, G. B., M.C. Prieto, G. Ricchiardi, V. Sanchez Escribano. On the Vibrational Spectra and Structure of FeCrO₃ and of the Ilmenite-Type Compounds CoTiO₃ and NiTiO₃. *Journal of Solid State Chemistry* **1994**, 112 (112), 9–14.
- (37) D. Renusch, B. V., K. Natesan & M. Grimsditch Transient oxidation in Fe-Cr-Ni alloys A Raman-scattering study. *Oxidation of Metals* **1996**, 46, 365–381.
- (38) Bhardwaj, P.; Singh, J.; Kumar, R.; Kumar, D.; Verma, V.; Kumar, R. Oxygen defects induced tailored optical and magnetic properties of Fe_xCr_{2-x}O₃ (0 ≤ x ≤ 0.1) nanoparticles. *Applied Physics A* **2022**, 128 (2), 135. DOI: 10.1007/s00339-021-05233-x.
- (39) Mehtani, H. K.; Khan, M. I.; Jaya, B. N.; Parida, S.; Prasad, M. J. N. V.; Samajdar, I. The oxidation behavior of iron-chromium alloys: The defining role of substrate chemistry on kinetics, microstructure and mechanical properties of the oxide scale. *Journal of Alloys and Compounds* **2021**, 871, 159583. DOI: 10.1016/j.jallcom.2021.159583.
- (40) Banerjee, I.; Kim, H. K. D.; Pisani, D.; Mohanchandra, K. P.; Carman, G. P. Magnetic anisotropy and magnetodielectric coefficients in Cr₂O₃ and Fe_{0.4}Cr_{1.6}O₃. *Journal of Alloys and Compounds* **2014**, 614, 305–309. DOI: 10.1016/j.jallcom.2014.06.038.
- (41) Liu, L. Z.; Li, T. H.; Wu, X. L.; Shen, J. C.; Chu, P. K. Identification of oxygen vacancy types from Raman spectra of Sn₂ nanocrystals. *Journal of Raman Spectroscopy* **2012**, 43 (10), 1423–1426. DOI: 10.1002/jrs.4078.
- (42) Yue, X.; Zhang, L.; Ma, L.; Lu, M.; Neville, A.; Hua, Y. Influence of a small velocity variation on the evolution of the corrosion

- products and corrosion behaviour of super ^{13}Cr SS in a geothermal CO_2 containing environment. *Corrosion Science* **2021**, 178, 108983. DOI: 10.1016/j.corsci.2020.108983.
- (43) Lin, H.-Y.; Chen, Y.-W.; Li, C. The mechanism of reduction of iron oxide by hydrogen. *Thermochimica Acta* **2003**, 400(1-2), 61-67. DOI: 10.1016/S0040-6031(02)00478-1. DOI: 10.1039/D5TA05111H
- (44) Kovalenko, V. V.; Rumyantseva, M. N.; Gaskov, A. M.; Makshina, E. V.; Yushchenko, V. V.; Ivanova, I. I.; Ponzoni, A.; Faglia, G.; Comini, E. $\text{SnO}_2/\text{Fe}_2\text{O}_3$ nanocomposites: Ethanol-sensing performance and catalytic activity for oxidation of ethanol. *Inorganic Materials* **2006**, 42 (10), 1088-1093. DOI: 10.1134/S0020168506100074.
- (45) Galvita, V.; Sundmacher, K. Redox behavior and reduction mechanism of $\text{Fe}_2\text{O}_3\text{-CeZrO}_2$ as oxygen storage material. *Journal of Materials Science* **2007**, 42 (22), 9300-9307. DOI: 10.1007/s10853-007-1872-7.
- (46) Wang, Y.-Q.; Li, Y.-X.; Fu, X.; Yue, J.-Y.; Cao, J.-W.; Ma, X.-B.; Liu, F.; Wang, J.-W. Catalytic oxidation of toluene by binary metal oxide $\text{Cr}_2\text{O}_3/\text{CeO}_2$ from MIL-101 (Cr). *Journal of Solid State Chemistry* **2023**, 328, 124334. DOI: 10.1016/j.jssc.2023.124334.
- (47) Festa, G.; Serrano-Lotina, A.; Meloni, E.; Portela, R.; Ruocco, C.; Martino, M.; Palma, V. Support Screening to Shape Propane Dehydrogenation SnPt-Based Catalysts. *Ind Eng Chem Res* **2024**, 63, 16269-16284. DOI: 10.1021/acs.iecr.3c04089
- (48) Tian, J.; Zheng, P.; Zhang, T.; Han, Z.; Xu, W.; Gu, F.; Wang, F.; Zhang, Z.; Zhong, Z.; Su, F.; et al. CO_2 methanation over Ni nanoparticles inversely loaded with CeO_2 and Cr_2O_3 : Catalytic functions of metal oxide/Ni interfaces. *Applied Catalysis B: Environmental* **2023**, 339, 123121. DOI: 10.1016/j.apcatb.2023.123121.
- (49) Xie, Z.; Yan, B.; Lee, J. H.; Wu, Q.; Li, X.; Zhao, B.; Su, D.; Zhang, L.; Chen, J. G. Effects of oxide supports on the CO_2 reforming of ethane over Pt-Ni bimetallic catalysts. *Applied Catalysis B: Environmental* **2019**, 245, 376-388. DOI: 10.1016/j.apcatb.2018.12.070.
- (50) Thapliyal, V.; Alabdulkarim, M. E.; Whelan, D. R.; Mainali, B.; Maxwell, J. L. A concise review of the Raman spectra of carbon allotropes. *Diamond and Related Materials* **2022**, 127, 109180. DOI: 10.1016/j.diamond.2022.109180.

The authors confirm that the data supporting the findings of this study are available within the article and its ESI

View Article Online
DOI: 10.1039/D5TA05111H

